Supporting Information for Dalton Trans 2021

Two chemically robust Cd(II)-frameworks for efficient sensing of levofloxacin, benzaldehyde, and Fe^{3+} ions

Yu-Qiao Su[a], Lianshe Fu[b], Guang-Hua Cui[a]*

[a]*College of Chemical Engineering, Hebei Key Laboratory for Environment Photocatalytic and Electrocatalytic Materials, North China University of Science and Technology, No. 21 Bohai Road, Caofeidian new-city, Tangshan, Hebei, 063210, P. R. China*

[b]*Department of Physics and CICECO-Aveiro Institute of Materials, University of Aveiro, 3810-193 Aveiro, Portugal*

Corresponding author: Guang-Hua Cui

Fax: +86-315-8805462. Tel: +86-315-8805460.

E-mail: tscghua@126.com

CONTENTS

Section 1. Experimental Section

1. Materials and physical measurements

2. Single crystal X-ray diffraction determination

3. Anti-interference experiments

4. Computational Details

5. Mott-Schottky curves measurements

6. Formulas

1. Materials and physical measurements

All chemicals and reagents were obtained from a commercial approach and used without further purification. Elemental analyses (C, H, and N) were carried out by a Perkin-Elmer 240C analyzer. FTIR spectra in the region of 4000−400 cm^{-1} were collected on the Bruker VERTEX 80V FTIR spectrophotometer. The morphologies of **1** and **2** were analyzed using a JEOL JSM-IT100 scanning electron microscope (SEM; JEOL Instruments, Tokyo, Japan) with a gold coating. Powder X-ray diffraction (PXRD) patterns were obtained on a Rigaku D/Max-2500PC diffractometer under the conditions of the X-ray tube of 40 kV and 40 mA with Cu target tube (λ = 1.5418 Å). Thermogravimetric analyses (TGA) of MOFs were investigated with a Netzsch STA449 F1 thermal analyzer in the air atmosphere with a heating rate of 10 °C/min in the range of 25–800 °C. Inductively coupled plasma mass spectrometry was conducted on a Varian model ICP spectrometer. The luminescence spectra were recorded on Edinburgh instruments FS5 spectrophotometer.

2. Single crystal X-ray diffraction determination

Crystallographic data for single crystals of **1** and **2** were collected on a Rigaku XtaLabMini diffractometer with Mo-Kα radiation (λ=0.71073 Å). The reflection data were processed by the CrysAlisPro program. [1] Structural analysis and data refinement were performed through the SHELXT-2015 and SHELXL-2018 programs. [2] The atomic coordinates and anisotropic parameters of the compound were refined by the full matrix least-squares method. Non-hydrogen atoms were treated anisotropically. The H atoms in water molecules were added by difference Fourier maps and with fixed displacement parameters. The other H atoms were geometrically

generated adopting a riding model and isotropically refined. Their primary crystallographic data are summarized in Table S1. The selected bonds distances and angles are listed in Table S2.

3. Anti-interference experiments

The anti-interference experiments were performed in the presence of the same concentration of levofloxacin (LEV) and other ions antibiotics (0.1 mM, amoxicillin (AMX), chlortetracycline (CTC), ciprofloxacin (CIP), doxycycline hyclate (DH), metronidazole (MDZ), nitrofurantoin (NFT), norfloxacin (NOR), oxytetracycline (OTC), ronidazole (RNZ), sulfadiazine (SDZ), sulfamethazine (SMZ), sulfamethoxazole (SMX), tetracycline (TC)). Anti-interference experiments for benzaldehyde recorded luminescence intensities of **1** and **2** (4 mg) in the presence of the analyte (2 ml) and other organics (2 ml) (acetonitrile (MeCN), cyclohexane (CY), dichloromethane (DCM), ethanol (EtOH), ethylene glycol (EG), glycol (GL), methanol (MeOH), n-butanol (NB), n-methyl pyrrolidone (NMP)). As for iron ions, Anti-interference sensing experiments were further implemented in EtOH/H_2O (1:1, v/v). The **1** or **2** powder was added to a mixed solution containing the Fe^{3+} ions and other metal ions (Na^+, K^+, Mg^{2+}, Ca^{2+}, Sr^{2+}, La^{3+}, Sm^{3+}, Gd^{3+}, Tb^{3+}, Er^{3+}, Pb^{2+}) at a concentration of 0.5 mM.

4. Computational Details

All calculations on electronic structures were carried out *via* ORCA 2.8 program [3]. Geometry optimizations was calculated through density functional theory (DFT). The frontier orbital energy of Cd(II) ions, free L1, L2, H_2tdc, and BZH were calculated by B3LYP/TZVP.[4–6] Molecular orbital visualization was analyzed by VMD 1.9.3 program. [7] The structural properties of the two Cd(II)-MOFs were calculated by Poreblazer v4.0 program (Table S3). [8]

5. Mott-Schottky curves measurements

Electrochemical measurements of the crystal materials were carried out at room temperature in a three-electrode cell. A CHI600A potentiostat connected to an analyzer was employed in the electrochemical measurements. Glassy carbon electrodes (GCE, Ø = 3 mm) were coated with the Cd(II)-MOFs as follows: 24 mg powders of the as-synthesized **1**–**2** were ultrasonicated in 4 mL ethanol for 2 h. Then, 30 μL of the suspensions were evenly spread on the surfaces of the GCE and dried in air for 30 min at room temperature. Next, 10 μL of 0.2% Nafion solution was quantitatively put onto the surfaces of the modified GCE. Finally, the Cd(II) complexes/GCE were obtained after drying air for about 1 h. Three electrode systems include Cd-MOFs **1**–**2** as the working electrode, respectively, a Pt-wire counter electrode and an Ag/AgCl reference electrode. The Mott-Schottky curves were measured in 0.1 M Na_2SO4 aqueous solution. The AC amplitude was set as 10 mV, and the frequency was 1000, 1500,2000 Hz.

6. Formulas

The Stern-Volmer (SV) plot

$$(I_0/I) = 1 + K_{sv}\,[M]$$

where I_0 and I are the maximum luminescent intensities before and after the addition of the targeted species, K_{sv} represents the quenching constant and [M] is the analyte concentration.

The low limit of detection (LOD)

$$LOD = 3\sigma/k$$

where σ stands for standard deviation, and k is the slope of the quenching curve.

The fluorescence lifetime

$$y(t) = B_1 e^{-t/\tau_1} + B_2 e^{-t/\tau_2}$$

which is obtained by a bi-exponential fit of the fluorescence decay data and where τ_1 and τ_2

represent the components of fluorescence lifetime, B_1 and B_2 are the corresponding amplitudes, and t is the instantaneous time.

The average fluorescence lifetime

$$\tau_{avg} = (B_1\tau_1^2 + B_2\tau_2^2)/(B_1\tau_1 + B_2\tau_2)$$

The conduction band (CB) and valence band (VB) positions

$$E_{VB} = E_{CB} - E_g$$

where E_{VB} is the VB potential, E_{CB} is the CB potential, and Eg is the bandgap energy of the crystal materials.

References

[1] CrysAlisPro, Oxford Diffraction/Agilent Technologies UK Ltd., Yarnton, UK.

[2] H. Erer, O. Z. Yesilel, and M. Arıcı, Cryst. Growth Des., 2015, 15, 3201−3211.

[3] F. Neese, Wiley Interdiscip. Rev. Sci., 2012, 2, 73−78.

[4] A. D. Becke, J. Chem. Phys., 1993, 5648.

[5] A. D. Becke, Phys. Rev., 1988, 38, 3098.

[6] O. Treutler, Re. Ahlrichs, J. Chem. Phys., 1995, 102, 346−354.

[7] W. Humphrey, A. Dalke, K. Schulten, J. Mol. Graphics, 1996, 14, 33−38.

[8] L. Sarkisov, R. B. Perez, M. Sutharson, D. F. Jimenez, Chem. Mater, 2020, 32, 9849−9867.

Section 2. Supplementary Tables and Figures

Scheme Titles:

Scheme S1 The chemical structures of different types of antibiotics.

Table Titles:

Table S1 Crystallographic data and refinement parameter for **1** and **2**.

Table S2 The selected bond lengths (Å) and angles (°) for **1** and **2**.

Table S3 The structural properties for **1** and **2**.

Figure Titles:

Fig. S1 One 1D double straight-line of metal Cd(II) growth by tdc^{2-} ligands.

Fig. S2 1D chain of metal Cd(II) growth by tdc^{2-} or L2 ligands.

Fig. S3 The infrared spectra of **1** and **2**.

Fig. S4. SEM images of the powdered **1** and **2**.

Fig. S5. The PXRD patterns for the simulated, synthesized samples, and removal of water molecules samples at 153℃ for **1**/**2**.

Fig. S6. TGA plots of complexes **1**–**2**

Fig. S7. Time-dependent luminescence emission spectra of **1** and **2** from 0 to 150 min by 15 min step (a) in water; (b) in EtOH.

Fig. S8. The change of the fluorescence emission intensities of **1** and **2** in different pH solutions.

Fig. S9 Plots for the selective detection of LEV over other antibiotics mentioned.

Fig. S10 Relative intensities for **1** and **2** immersed in the individual solvents and mixtures of competing solvents including BZH.

Fig. S11. Comparison of the fluorescence emission intensities of **1**/**2** for sensing Fe^{3+} ions (5×10^{-4} M) in the presence of other ions (5×10^{-4} M).

Fig. S12. The luminescence intensities of **1**/**2** for sensing LEV (a), BZH (b), and Fe^{3+} ions (c) over three cycles; (d) PXRD patterns of the simulated of **1**/**2** after sensing for three cycles.

Fig. S13. Mott−Schottky plots for the two as-prepared materials in 0.1 M Na_2SO4 aqueous solution. AC amplitude is 10 mV, and the frequency is 1000, 1500, and 2000 Hz, respectively

Fig. S14. Diffuse reflectance spectra of Kubelka–Munk function *vs*. energy of **1**–**2.**

Fig. S15. Schematic band structures of **1**, **2**, LEV, BZH, and Fe^{3+} ions.

Fig. S16. Fluorescence excitation/emission spectra of **1**/**2** and UV–Vis absorption spectra of selected analytes.

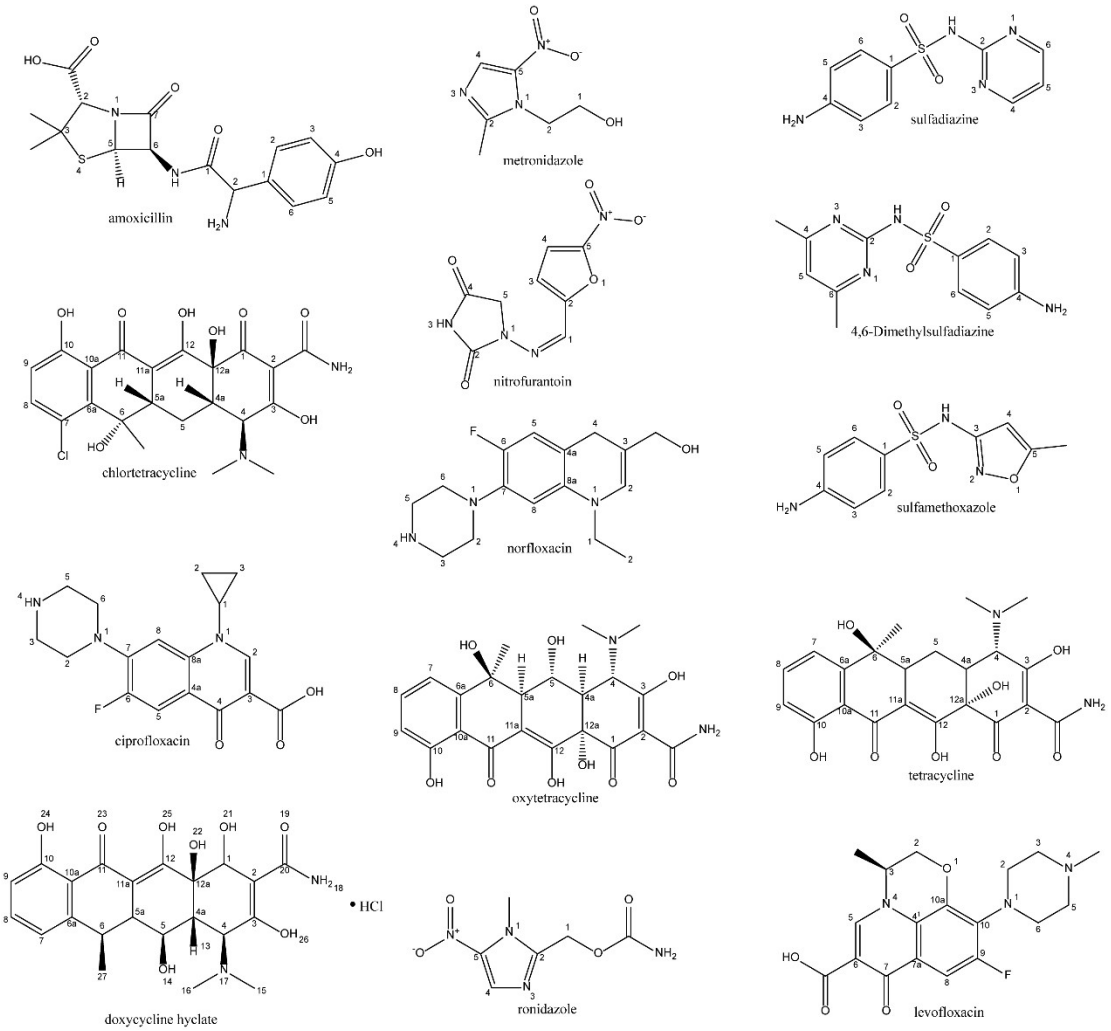

Scheme S1 The chemical structures of different types of antibiotics.

Table S1 Crystallographic data and refinement parameter for **1** and **2**.

MOF	**1**	**2**
Chemical formula	$[Cd_2(L1)(tdc)_2(H_2O)]_n$	$[Cd(L)_{0.5}(tdc)]_n$
Formula weight	1085.70	532.85
Crystal system	monoclinic	monoclinic
Space group	I_2/a	$P2_1/n$
a (Å)	23.9212(9)	10.1950(12)
b (Å)	10.3352(3)	21.3148(15)
c (Å)	34.8506(15)	10.7401(9)
α (°)	90	90
β (°)	90.661(4)	117.238(13)
γ (°)	90	90
V (Å^3)	8615.6(6)	2075.1(4)
Z	8	4
D_{calcd} (g/cm^3)	1.674	1.706
Absorption coefficient, mm^{-1}	1.150	1.188
F(000)	4352	1068
Crystal size, mm	0.26×0.25×0.24	0.26×0.24×0.22
θ range, deg	4.108–60.96	4.674–61.006
Index range h, k, l	–33/33, –14/14, –49/49	–14/14, –29/29, –15/15
Reflections collected	116794	27549
Independent reflections (R_{int})	12823 (0.0633)	5984(0.0362)
Data/restraint/parameters	12823/0/570	5984/0/280
Goodness–of–fit on F^2	1.159	1.072
Final R_1, wR_2 ($I > 2\sigma(I)$)	0.0439, 0.0981	0.0319, 0.0735
Largest diff. peak and hole	0.95, –1.25	0.55, –1.32

Table S2 The selected bond lengths (Å) and angles (°) for **1** and **2**.

Parameter	Value	Parameter	Value
1			
Cd1–O9	2.337(3)	O9–Cd1–O8A	86.34(1)
Cd1–O1	2.324(3)	O1–Cd1–O8A	88.83(1)
Cd1–O7A	2.440(3)	O7A–Cd1–O8A	54.94(1)
Cd1–O8A	2.317(3)	O8A–Cd1–N1	143.71(1)
Cd1–O5	2.189(3)	O5–Cd1–O9	85.45(1)
Cd2–N1	2.327(3)	O5–Cd1–O1	99.83(1)
Cd2–O4A	2.492(3)	O5–Cd1–O7A	167.04(1)
Cd2–O10	2.304(3)	O5–Cd1–O8A	123.31(1)
Cd2–O2	2.219(3)	O5–Cd1–N1	92.23(1)
Cd2–O3A	2.260(3)	O9–Cd1–N1	89.83(1)
Cd2–N6B	2.390(3)	O7A–Cd1–N1	88.80(1)
Cd2–N3B	2.334(3)	O10–Cd2–O4A	89.96(1)
O9–Cd1–O7A	81.64(1)	O10–Cd2–O4A	89.96(1)
O1–Cd1–O9	174.25(1)	O10–Cd2–N6B	82.41(1)
O1–Cd1–O7A	93.03(1)	O10–Cd2–N3B	161.14(1)
O1–Cd1–N1	92.23(1)	O2–Cd2–O4A	166.54(1)
2			
Cd1–O2	2.293(2)	N1–Cd1–N3B	92.21(1)
Cd1–O1	2.450(2)	N3B–Cd1–O1	123.66(1)
Cd1–O4A	2.329(2)	O3A–Cd1–O1	142.02(1)
Cd1–O3A	2.347(2)	O3A–Cd1–N3B	88.61(1)
Cd1–N1	2.270(2)	N1–Cd1–O2	136.66(1)
Cd1–N3B	2.370(2)	N1–Cd1–O1	96.17(1)
O2–Cd1–O1	55.28(1)	N1–Cd1–O4A	120.97(1)
O2–Cd1–O4A	91.46(1)	N1–Cd1–O3A	102.60(1)
O2–Cd1–O3A	120.01(1)	O4A–Cd1–O3A	56.20(1)
O2–Cd1–N3B	81.75(1)	O4A–Cd1–N3B	134.35(1)

Symmetry codes for **1**: A = *x*, *y*+1, *z*; B = 0.5+*x*, 2–*y*, *z*; for **2**: A = 0.5+*x*, 0.5–*y*, *z*–0.5; B = 2–*x*, 1–*y*, –*z*; C = 2–*x*, 1–*y*, 1–*z*.

Table S3 The structural properties for **1** and **2**.

property	**1**	**2**
accessible surface area, m^2/g	3295.07	3550.37
geometric pore volume, cm^3/g	1.21	1.23
probe-occupiable volume, cm^3/g	1.10	1.10
helium pore volume, cm^3/g	0.91	0.84
pore limiting diameter, Å	6.97	4.62
largest cavity diameter, Å	8.60	5.77

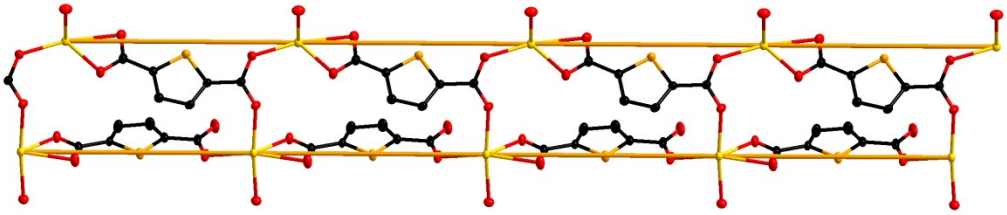

Fig. S1 One 1D double straight-line of metal Cd(II) growth by tdc^{2-} ligands.

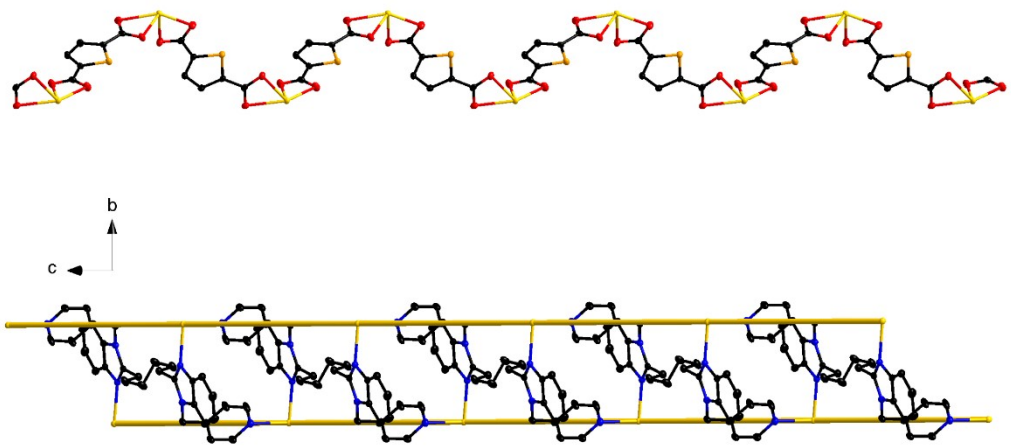

Fig. S2 1D chain of metal Cd(II) growth by tdc^{2-} or L2 ligands.

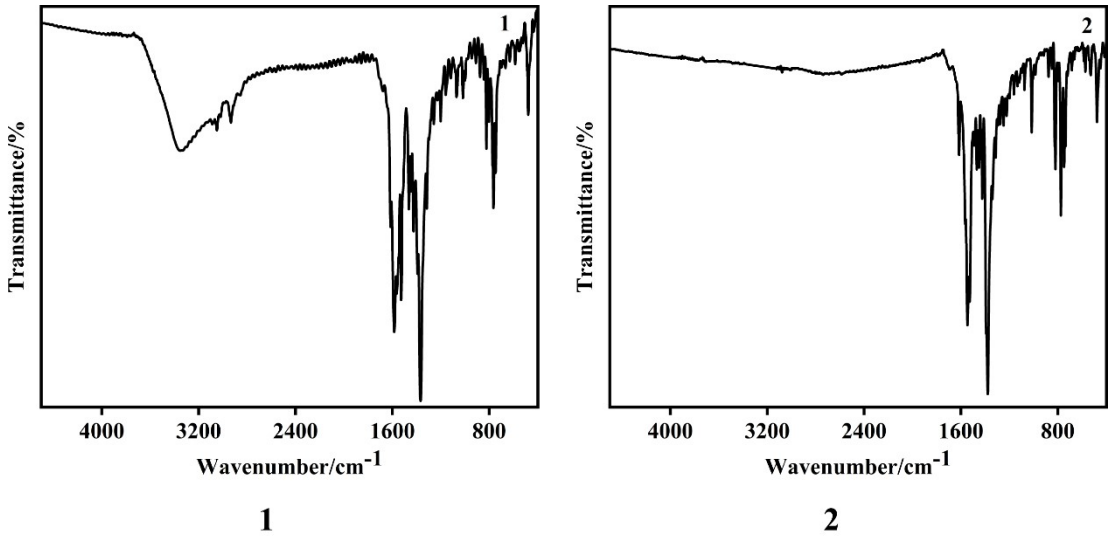

1 **2**

Fig. S3 The infrared spectra of **1** and **2**.

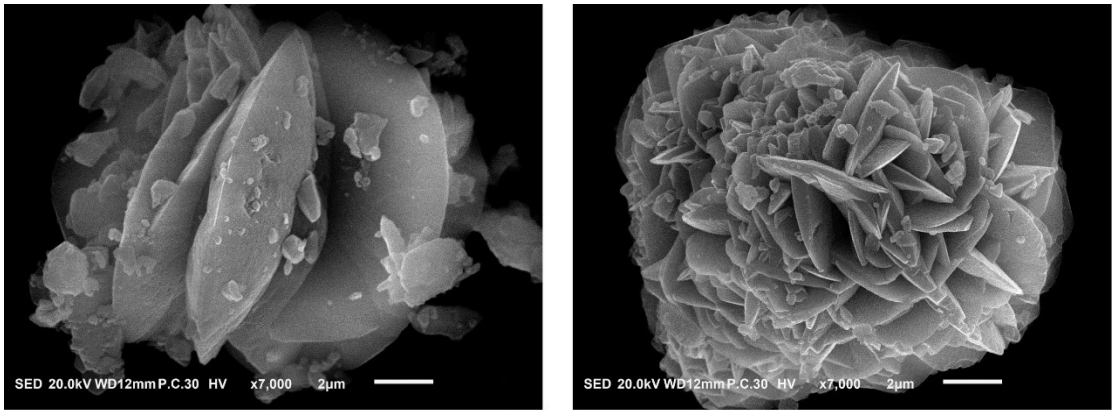

1 **2**

Fig. S4. SEM images of the powdered **1** and **2**.

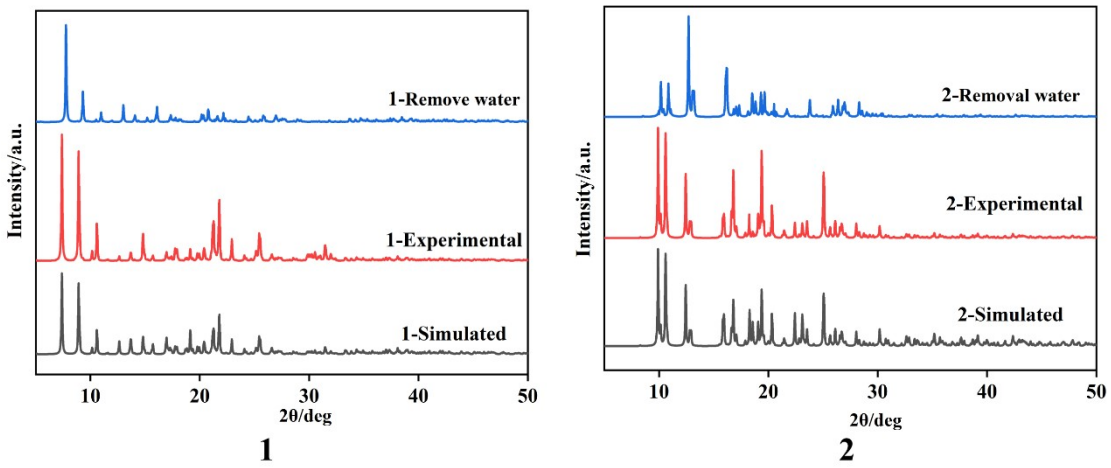

Fig. S5. The PXRD patterns for the simulated, synthesized samples, and removal of water molecules samples at 153℃ for **1**/**2**.

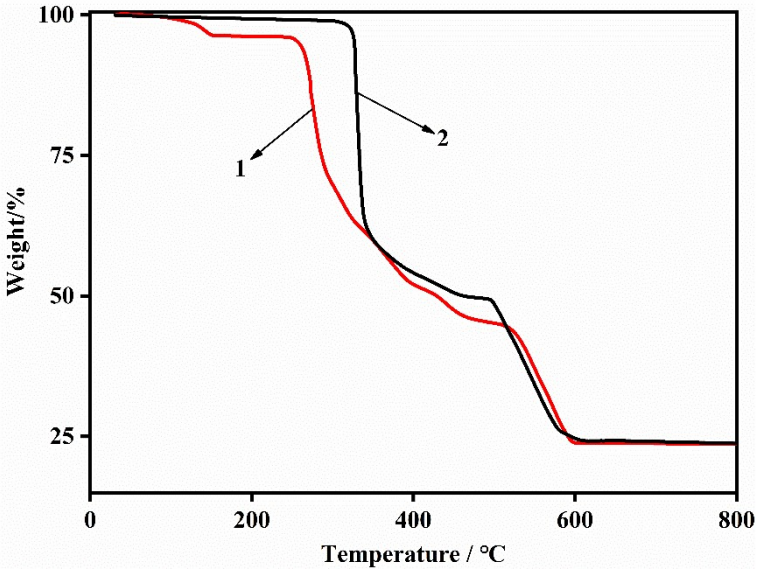

Fig. S6. TGA plots of complexes **1**–**2**

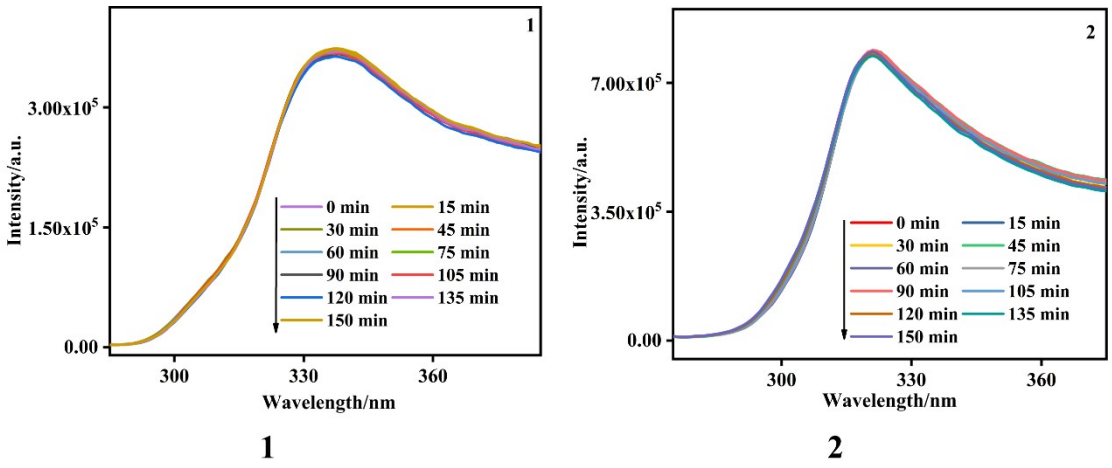

(a)

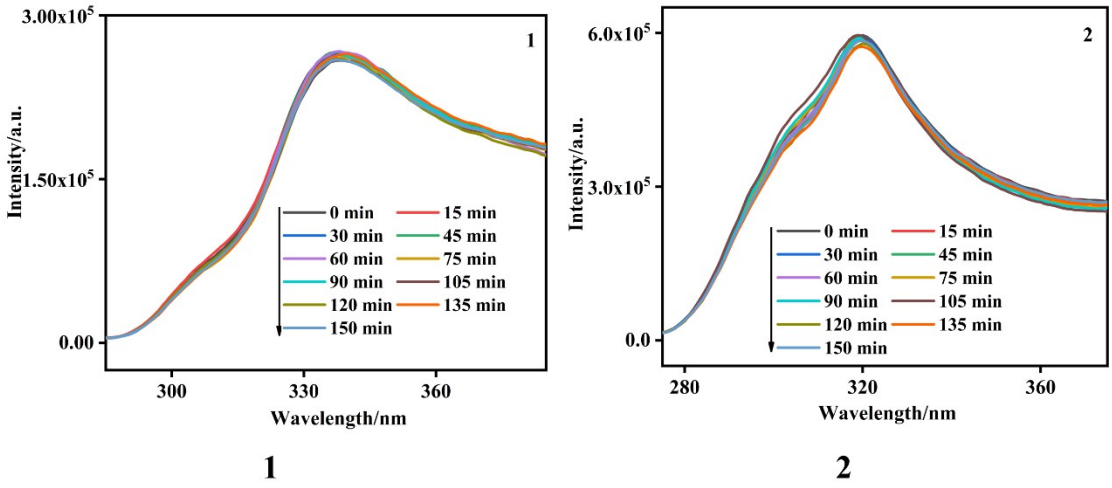

(b)

Fig. S7. Time-dependent luminescence emission spectra of **1** and **2** from 0 to 150 min by 15 min step (a) in water; (b) in EtOH.

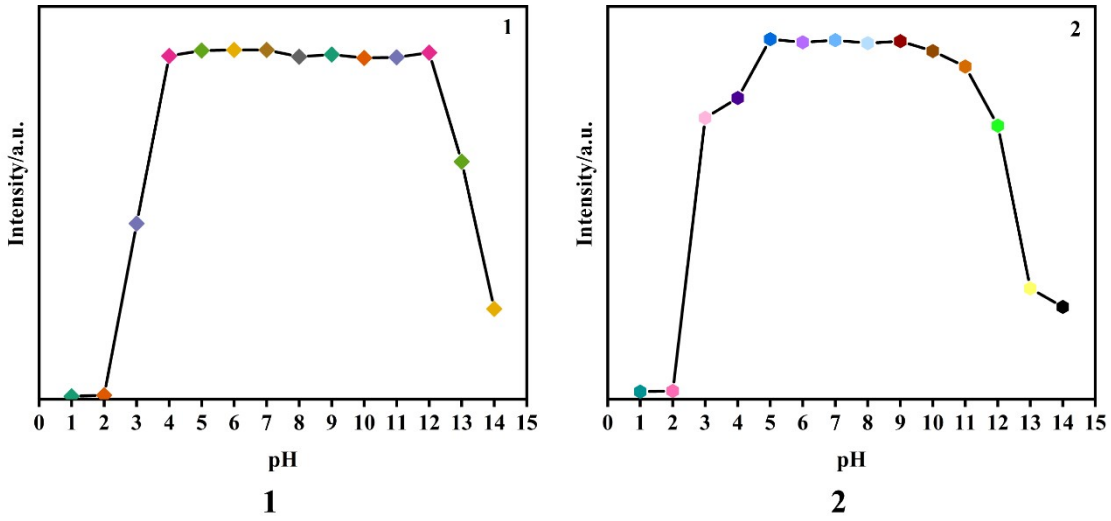

Fig. S8. The change of the fluorescence emission intensities of **1** and **2** in different pH solutions.

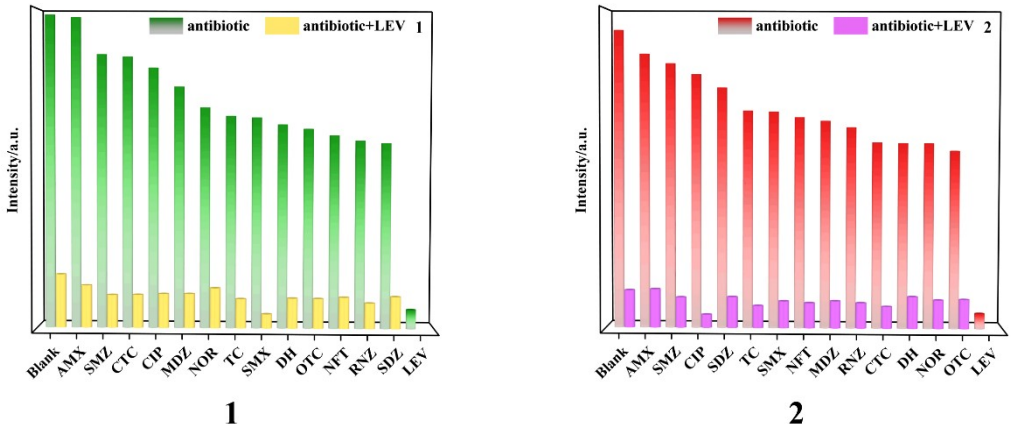

Fig. S9 Plots for the selective detection of LEV over other antibiotics mentioned.

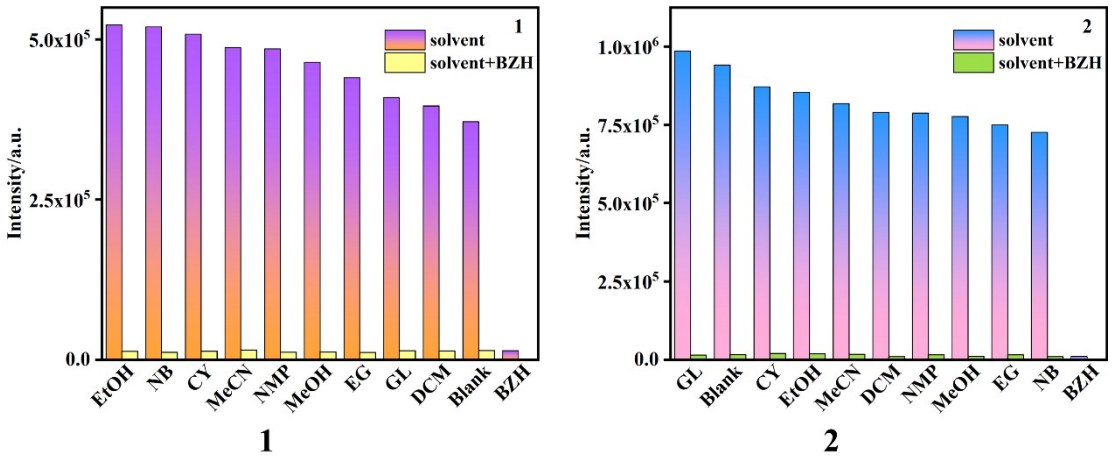

Fig. S10 Relative intensities for **1** and **2** immersed in the individual solvents and mixtures of competing solvents including BZH.

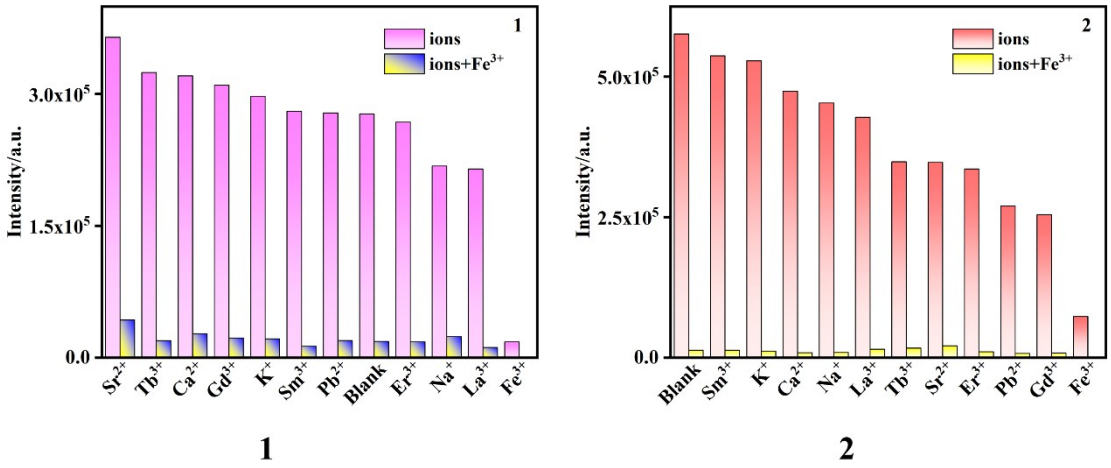

Fig. S11. Comparison of the fluorescence emission intensities of **1**/**2** for sensing Fe^{3+} ions (5×10^{-4} M) in the presence of other ions (5×10^{-4} M).

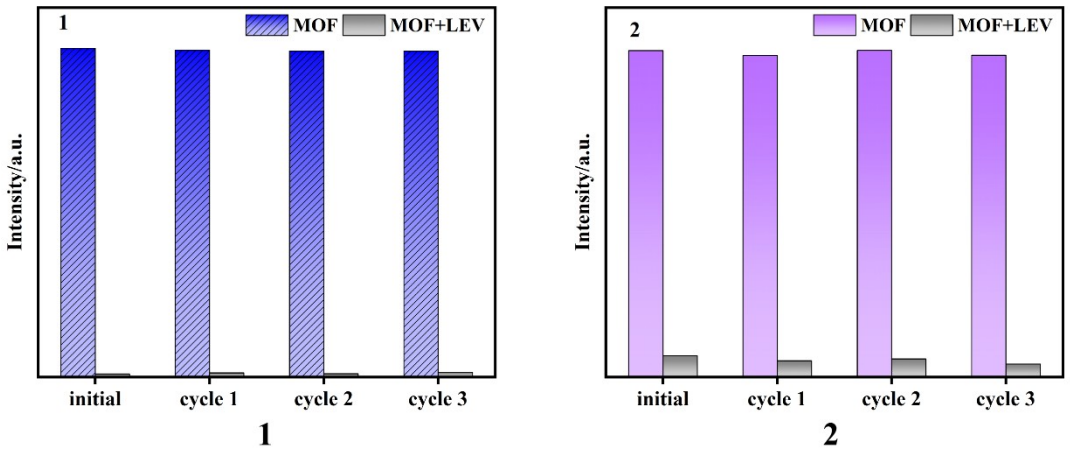
1
MOF
MOF+LEV
Intensity/a.u.
initial
cycle 1
cycle 2
cycle 3
1
2
MOF
MOF+LEV
Intensity/a.u.
initial
cycle 1
cycle 2
cycle 3
2

(a)

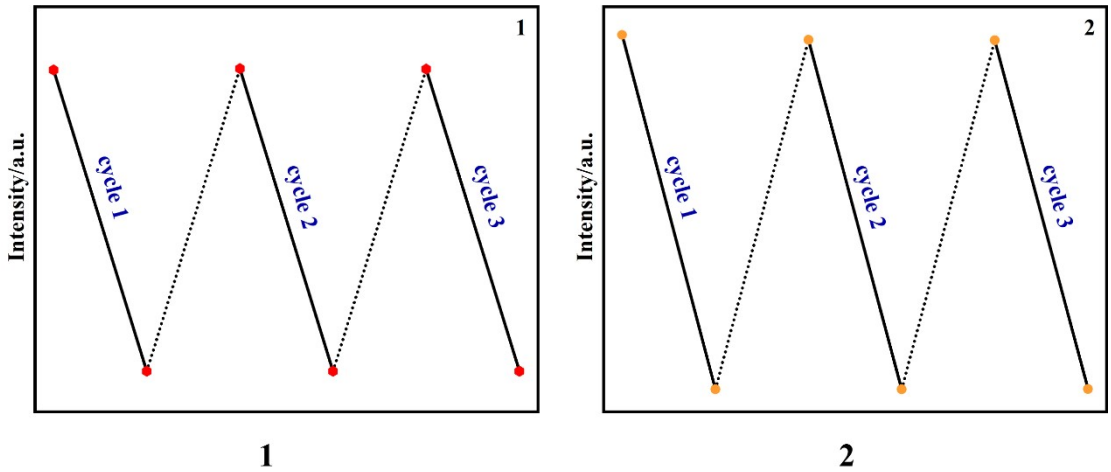
1
Intensity/a.u.
cycle 1
cycle 2
cycle 3
1
2
Intensity/a.u.
cycle 1
cycle 2
cycle 3
2

(b)

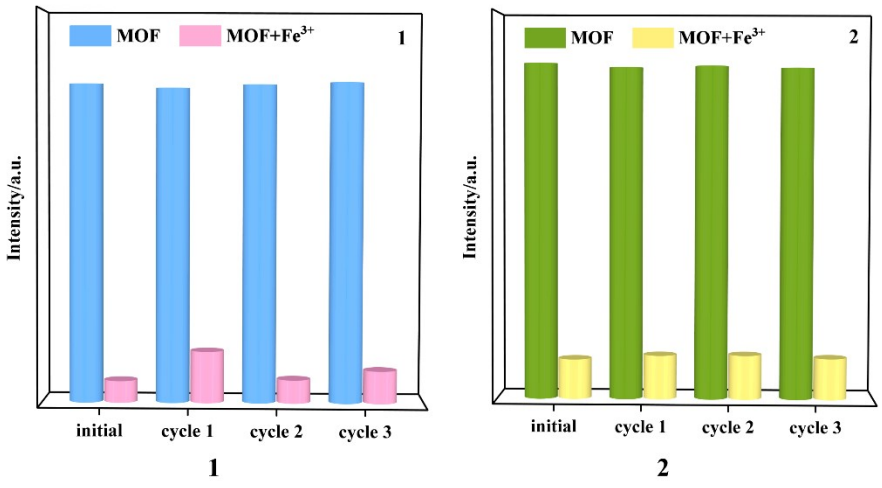
MOF
MOF+Fe3+
1
Intensity/a.u.
initial
cycle 1
cycle 2
cycle 3
1
MOF
MOF+Fe3+
2
Intensity/a.u.
initial
cycle 1
cycle 2
cycle 3
2

(c)

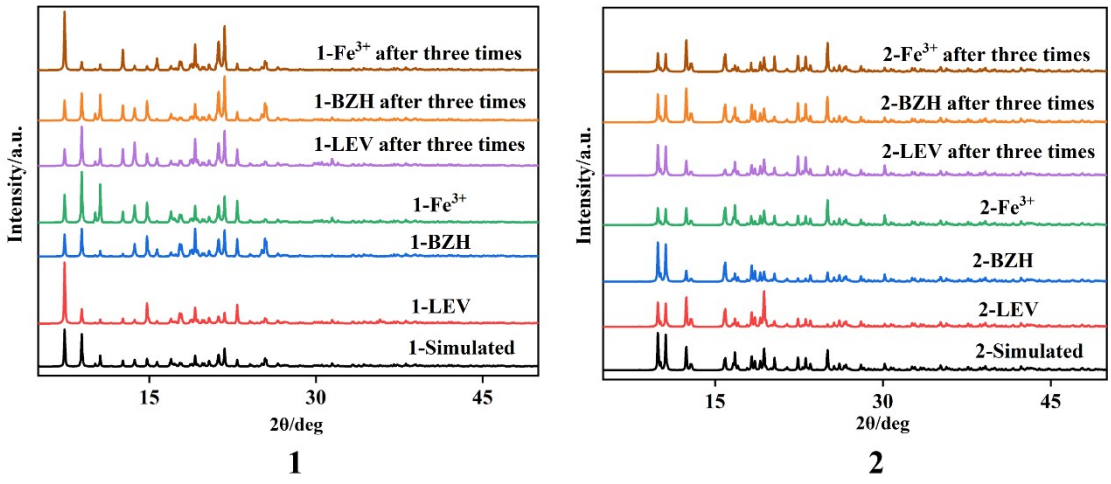

(d)

Fig. S12. The luminescence intensities of **1**/**2** for sensing LEV (a), BZH (b), and Fe^{3+} ions (c) over three cycles; (d) PXRD patterns of the simulated of **1**/**2** after sensing for three cycles.

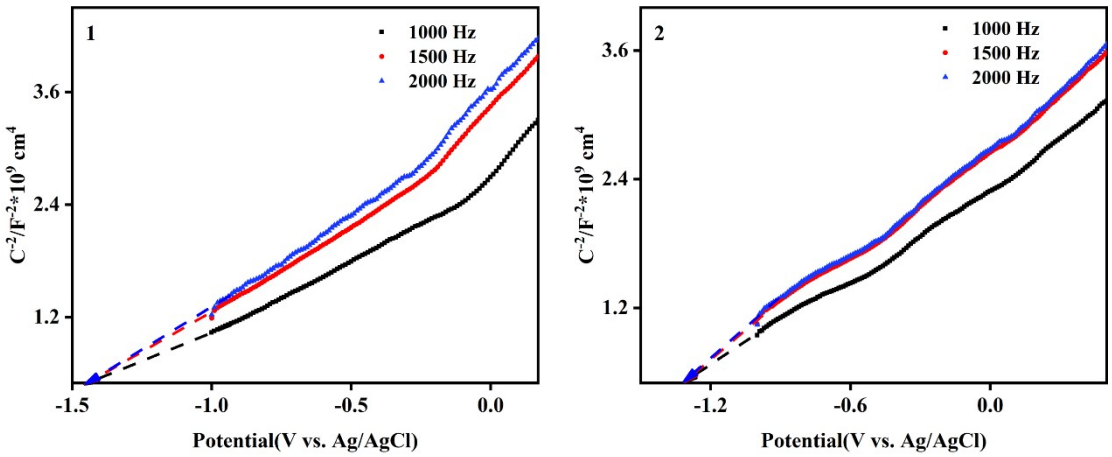

1 **2**

Fig. S13. Mott−Schottky plots for the two as-prepared materials in 0.1 M Na_2SO4 aqueous solution. AC amplitude is 10 mV, and the frequency is 1000, 1500 and 2000 Hz, respectively

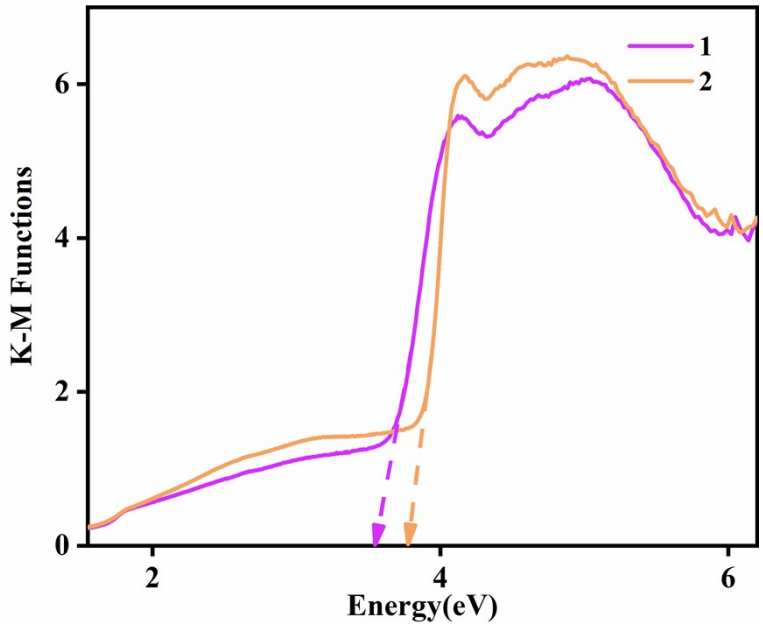

Fig. S14. Diffuse reflectance spectra of Kubelka–Munk function *vs*. energy of **1**–**2.**

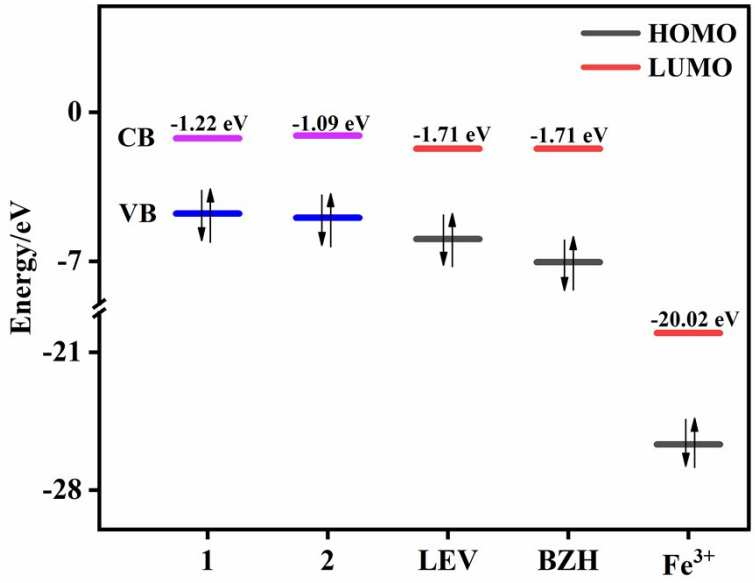

Fig. S15. Schematic band structures of **1**, **2**, LEV, BZH, and Fe^{3+} ions.

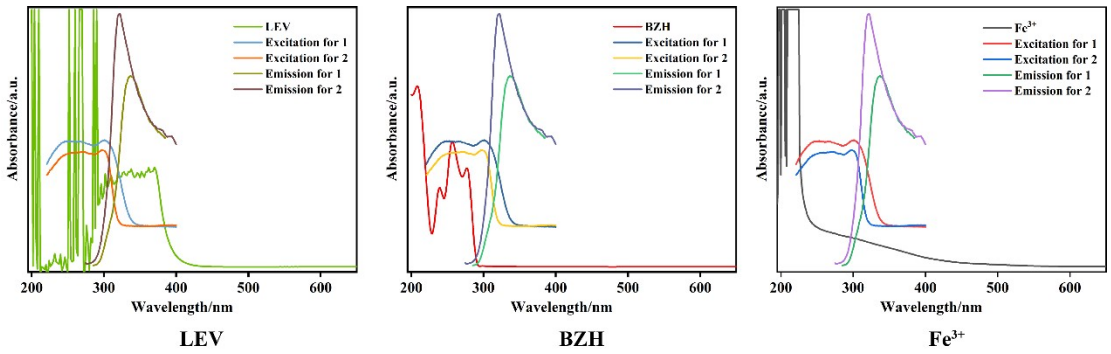

Fig. S16. Fluorescence excitation/emission spectra of **1**/**2** and UV–Vis absorption spectra of selected analytes.

Section 3. Supplementary Characterizations

IR spectra

The broadband (3352 cm^{-1} in **1**) is observed in the IR spectrum, and it is attributed to O–H vibrations of coordinated water molecules. There is no characteristic C=O stretching mode of carboxylic acids near 1700 cm^{-1}, indicating that the O-donor H_2tdc ligands are entirely deprotonated. The absorption peaks around 1584, 1563, 1426, 1367 cm^{-1} for **1** and 1547, 1528 cm^{-1} for **2** are attributed to the asymmetric (ν_{as}(COO)) and symmetric (ν_s(COO)) vibrations of the carboxylate groups, respectively. The separations $\Delta\nu[\nu_{as}(COO)-\nu_s(COO)]$ reveal the presence of the coordination modes of monodentate (217 cm^{-1} for **1**), bridging (158 cm^{-1} for **1**) and chelating (21 cm^{-1} for **1**, 19 cm^{-1} for **2**) types. The characteristic bands at (1526 cm^{-1} for **1**, 1528 cm^{-1} for **2**) are assigned to the $\nu_{C=N}$ stretching vibrations of the bis(pyridylbenzimidazole)-based ligands.

Optical band gaps

The diffuse reflectance data of the complexes **1**–**2** are transformed into Kubelka–Munk function to obtain their band gaps (E_g). These values were determined as the intersection point between the energy axis and the line extrapolated from the linear portion of the adsorption edge in a plot of the Kubelka–Munk function F against energy E. The Kubelka–Munk function ($F = (1 - R)^2/2R$) was transformed from the diffuse reflectance data, where R reflects an infinitely thick layer at a given wavelength.[9] The E_g values assessed from the steep absorption edge were 3.55 eV for **1**, 3.87 eV for **2** (Fig. S14).

References

[9] Z. W. He, C. J. Liu, W. D. Li, S. S. Han, S. S. Chen, Crystals, 2019, 9, 601.